Geochemical Profiles of Three Deep-sea Hydrothermal Plumes of the Eastern Lau Spreading Center

Kathleen Wendt[1]*, Jeffery V. Sorensen[1], Houshou Jiang[3], Gregory J. Dick[2], John A. Breier[3], and Brandy M. Toner[1]

[1]University of Minnesota [2]University of Michigan [3]Woods Hole Oceanographic Institute

*Corresponding author: wendt095@umn.edu

Inputs from deep-sea hydrothermal vents influence ocean geochemical budgets worldwide. Hydrothermal vents produce buoyant and chemically dynamic plumes that are rich in trace seawater elements. The mineral diversity in lower plumes is a direct result of interactions between local geology, hydrology, and biology. Because of this, differences in geochemical trends among naturally occurring plumes are detectable. Past studies have focused on geologic and bulk-chemistry differences between hydrothermal vents (Ferrini et al. 2008; Baker et al. 2005; Pearce et al. 1995; Tivey et al. 2005), while mineral differences among individual plumes remain poorly understood. This study examines and compares lower plume geochemistry of three hydrothermal vents located along the Eastern Lau Spreading Center (ELSC). Deep-sea hydrothermal plumes were sampled by *in-situ* filtration using *ROV Jason2* and the *SUPR Sampler* (Breier et al. 2009). Samples were collected 0.5 meters above each vent onto polycarbonate membrane filters. Plume particles on the filters were examined by synchrotron radiation X-ray fluorescence (XRF) mapping. Subsequently, a total of 67 filter-bound particles underwent X-ray ray diffraction (XRD) to define the crystalline minerals. Differences among sites are compared and discussed regarding: (1) geologic setting; (2) vent fluid chemistry; and (3) lower-plume mineral species. Reduced metal polysulfides were detected in concentrations that coincide with previous bulk-chemistry studies (Mottl et al., 2011; Tivey et al., 2007; Ishibashi and Urabe, 1995). In addition, this study will introduce a new method to rate confidence levels associated with the identification of mineral species using X-ray microprobe XRD and XRF analysis.

Introduction

The Lau Basin is located adjacent to the Australian-Pacific convergent plate boundary in the South Pacific Ocean. A combination of geologic processes allow for favorable spreading-center formation, including: (1) the stretching and thinning of overlying Australian plate boundary due to trench rollback processes, and (2) an uprising melt from the westward-dipping

Tonga-Kermadec subduction zone (Ishibashi, 2006). The resulting Lau Basin can be divided into four major spreading centers: the Northern, Center, Intermediate, and Eastern Lau Spreading Centers. Each spreading center is characterized by unique geology, spreading rates, and hydrothermal activity due to proximity to volcanic arc front (Pearce et al., 1995).

The Eastern Lau Spreading Center

The Eastern Lau Spreading Center (ELSC), as seen in figure 1, stretches across 400 km and is comprised of three morphologically distinct tectonic segments (Macdonald et al., 1991; Zellmer and Taylor, 2001; Martinez et al. 2006). The northern-ELSC begins at 20.6°S with a spreading rate of 96 mm/yr and an axial depth of 2500-3000 m. Northern-ELSC is dominated by basalt rock of pillow lava texture. The central-ELSC is separated by a 2.5 km offset with decreased spreading rates of 61-75 mm/yr. An axial magma chamber located throughout a majority of ELSC reaches its depth of 2-2.5 km below the seafloor at the central-ELSC. Pillow and lobate lava landscapes dominate central-ELSC. The southernmost segment, labeled Valu Fa Ridge (VFR), is the shallowest portion of the ELSC spreading at a decreased rate of 31-61 mm/yr. The VFR axial magma chamber dips to 2.7-3 km below the seafloor. Petrologic studies show felsic volcanic activity in the VFR, ranging from basalt enriched lithophile elements to andesite. Local host rock exhibits abundant vesicles due to high gas content in VFR magma. (Jacobs et al., 2007).

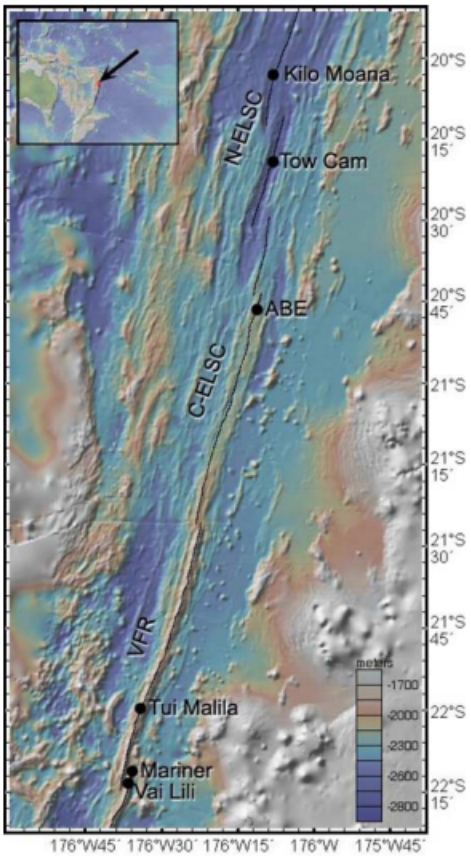

Figure 1: Eastern Lau Basin (Ferrini et al., 2008)

Overall, ELSC is characterized by a deep flat axial valley in the north with a transition to a shallow, narrower, peaked axial ridge in the south (Martinez et al., 2006; Jacobs et al., 2007). Morphology differences have been attributed to the increasing proximity to the subduction zone from south to north, thus affecting mantle chemistry (Martinez et al., 2006). In addition to morphology, six main differences between south and north ELSC have been observed:

i. A south to north increase in spreading rates. Spreading rates are relatively high (96 mm/yr) in the north and slower in the south (31-61 mm/yr) due to increasing subduction zone proximity (Zellmer and Taylor, 2001);
ii. Bathymetry infers a south to north increase in magmatic productivity associated with decreasing distances between the spreading axis and volcanic arc front (Martinez et al., 2006);
iii. A south to north increase in magma silica content (Pearce et al., 1995; Bezos et al., 2005);
iv. Regional surveys of seafloor have shown a decreasing degree of faulting and fissuring towards the south ELSC (Martinez et al., 2006);
v. A decrease in acoustic backscatter intensity toward the south ELSC implies an increase in sediment cover (Martinez et al., 2006);
vi. A south to north increase in hydrothermal plume incidence (Baker et al., 2006).

Hydrothermal venting

The geochemical inputs from hydrothermal venting systems influence geochemical budgets throughout entire ocean basins (Tivey et al., 2007; German and Vonn Damm, 2003; Mottl et al., 2011). The chemical composition of hydrothermal fluid provides an integrated record of the reactions and pressure-temperature conditions this fluid underwent during its passage through the crust. Because of this, hydrothermal fluids generated by venting systems act as a window into subsurface crustal processes. Determining the magnitude of their flux and overall importance in controlling ocean chemistry has, thus, become of interest to a variety of authors (Brier et al., 2012; Ferrini et al., 2008; Tivey et al., 2007; German and Vonn Damm, 2003; Mottl et al., 2011).

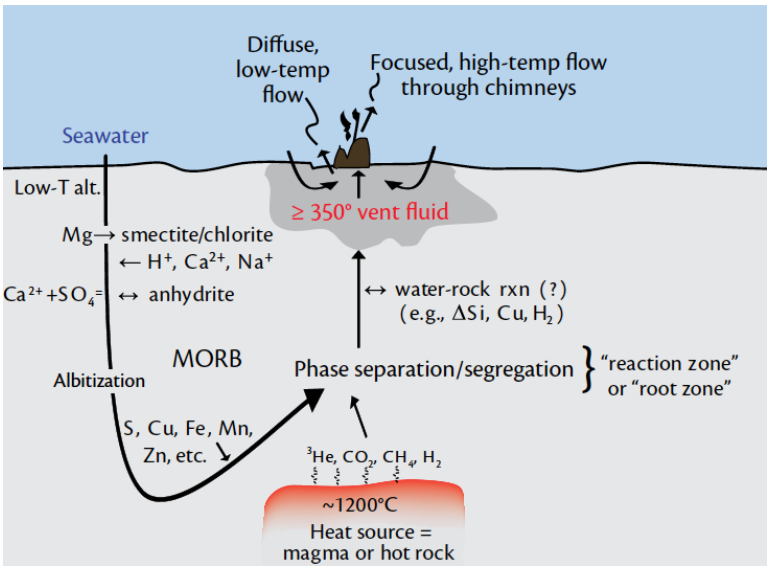

Figure 2: Hydrothermal process (Tivey et al., 2007)

Hydrothermal vents are the result of sub-seafloor hydrothermal circulation. Hydrothermal circulation occurs where seawater penetrates the Earth's crust through fractures and fissures near spreading centers. The downward moving seawater is heated by the underlying magma well and chemically altered through a series of seawater-to-host rock reactions. Heating causes the loss of dissolved sulfate (SO_4^{2-}) as anhydrite ($CaSO_4$) precipitates. Heating also promotes the loss of magnesium (Mg^{2+}) due to the formation of hydroxide-bearing silicates, subsequently generating protons (H^+) that contribute to low pH and reduction of alkalinity. As seawater continues to pass through the hydrothermal system, it reacts with local host rock and sediment substrates (German and VonDamm, 2003; Edmond et al., 1979; W. Seyfried, 1987; M.K. Tivey, 2007). This process promotes the enriching of hydrothermal fluids in dissolved metals, such as iron (Fe^{2+}) and manganese (Mn^{2+}) (Elderfield and a. Schultz, 1996; German and Vonn Damm, 2003).

The resulting end-member fluid, both thermally and chemically altered, ascends again and is expelled through hydrothermal vent structures. As fluid is transported through chimney structures, the chemical composition of this structure may contribute mineral species to end-member fluids (Haymon 1983). Overall, expelled fluids represent the net result of all reactions that have occurred along the entire hydrothermal flow path. Every hydrothermal vent that has been discovered, thus far, contains chemically different end-member hydrothermal fluids (VonDamm, 1995). The geochemical diversity of end-member fluid is hypothesized to be the direct result of local chemistry, geology, hydrology, and microbiology variations.

Bulk concentrations of end-member hydrothermal fluids have been examined by a number of authors (Ishibashi and Urabe 1995; Landing and Bruland, 1987; Von Damm, 1995; Cowen et al., 2001) (Figure 3). End-member fluid trace metals, such as V, CO, Ni, Cu, Zn, As, Se, Al, Ag, Cd, Ce, Au, and Pb, are enriched relative to seawater by 7 to 8 orders of magnitude (German and Von Damm, 2003). The two metals most enriched in hydrothermal vent fluids are iron (Fe^{2+}) and manganese (Mn^{2+}), reaching up to 100 orders of magnitude higher than ambient water column values (Mottl et al., 2011). Both elements are present as reduced dissolved form in end-member fluid and later oxidize and precipitate in hydrothermal plumes.

	Back-Arc
T (°C)	278–334
pH (25°C)	< 1–5.0
Cl, mmol/kg	255–790
Na, mmol/kg	210–590
Ca, mmol/kg	6.5–89
K, mmol/kg	10.5–79
Ba, µmol/kg	5.9–100
H_2S, mmol/kg	1.3–13.1
H_2, mmol/kg	0.035–0.5
CO_2, mmol/kg	14.4–200
CH_4, mmol/kg	.005–.06
NH_3, mmol/kg	-
Fe, µmol/kg	13–2500
Mn, µmol/kg	12–7100
Cu, µmol/kg	.003–34
Zn, µmol/kg	7.6–3000
Pb, µmol/kg	0.036–3.900
Co, µmol/kg	-
Cd, µmol/kg	-
Ni, µmol/kg	-
SO_4, mmol/kg	0
Mg, mmol/kg	0

Figure 3: Element concentrations of back-arc hydrothermal venting systems presented in mmol/kg as compared to standard seawater concentrations (Ishibashi and Urabe 1995)

When metal-rich end member fluid first enters the cold, oxic, deep-ocean a number of processes occur. First, the fluids are cooled causing the precipitation of a range of metal sulfide phases. These lower-plume phases are rich in Fe and to a lesser degree Mn, since Mn does not as readily form sulfide minerals (German and Von Damm 2003). Zinc (Zn) is 1-6 orders of magnitude less concentrated than Fe in hydrothermal fluids, however, Zn sulfide minerals also form rapidly in hydrothermal plumes (German and Vonn Damm, 2003). As the vent fluids mix with near bottom seawater, they form a turbulent rising plume that entrains large volumes of the surrounding seawater (Lupton et al., 1985). The mixing of the reduced and hydrogen sulfide (H_2S)-rich hydrothermal fluid with the oxic seawater creates chemical gradients across which many oxidation reactions occur. Iron oxides form rapidly in plumes once H_2S is consumed. In contrast, dissolved Mn exhibits slower oxidation kinetics, thus remaining as $Mn^{2+}{}_{(aq)}$ for longer periods of time in the deep ocean.

Understanding the mechanisms of mineral formation in hydrothermal plumes is important, as it provides insight to: (1) crustal dynamics and processes, (2) deep ocean microbial metabolism and ecology, and (3) global geochemical input from hydrothermal plumes to oceans. The fate of hydrothermal Fe in the ocean is of particular interest due to its important role in sustaining a marine primary productivity (Tagliabue et al. 2010)

Hydrothermal Venting at the ELSC

The Eastern Lau Spreading Center is characterized by a wide variety of hydrothermal vent fields. This study will focus on three vent sites: Kilo Moana, ABE, and Mariner. Differences between sites are summarized in table (1).

Table 1: ELSC vent comparison (Mottl et al., 2011; Tivey et al., 2007; Ferrini et al., 2008)

Vent Name	ELCS location	Temp-eratures	Depth	Depth to magma lens	Distance to arc	Substrate	Chimney Composition	Hydrothermal activity process
Kilo Moana	Northern	333°C	2620m	No lens	95m	Basalt	Chalcopryite ($CuFeS_2$) and wurtzite (ZnS)	Faulting
ABE	Central	309°C	2220m	2.0 km	70m	Basalt-andesite	Chalcopryite and wurtzite	Faulting
Mariner	Southern	363°C	1910m	2.8 km	50m	Basalt-andesite	Chalcopryite	Magmatic

The following vent descriptions are ordered from north to south ELSC:

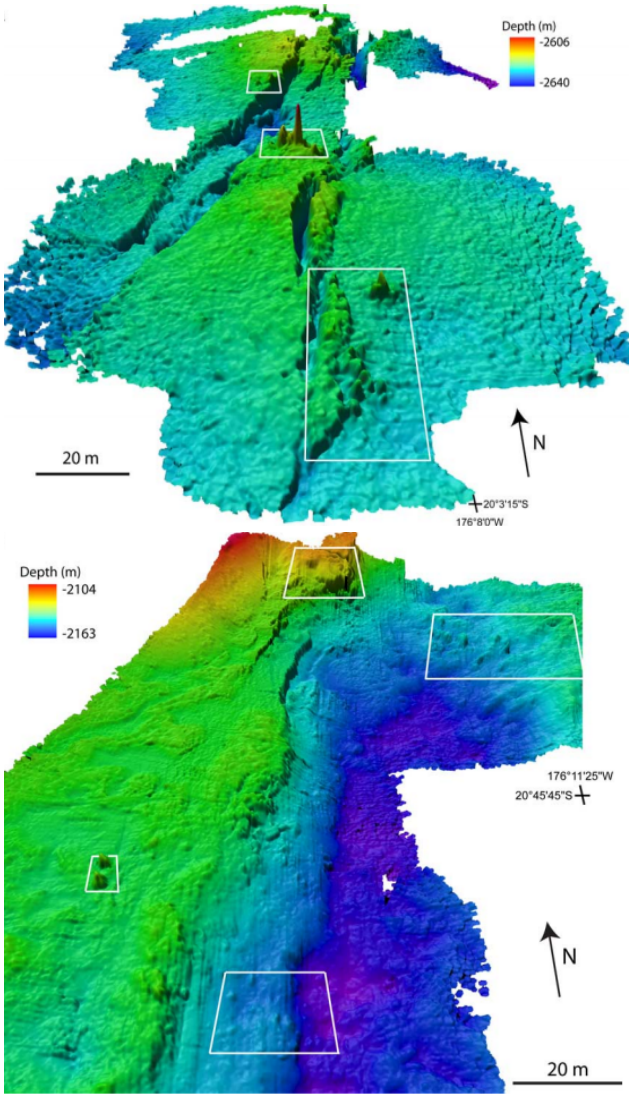

Figure 4 (top): Bathymetry map of Kilo Moana vent site (Ferrini et al., 2008). Figure 5 (bottom): Bathymetry map of ABE vent site (Ferrini et al., 2008).

KiloMoana

Kilo Moana (figure 4) is located 500m west of the northern-ELSC spreading axis on a slightly asymmetric bathymetric high (Ferrini et al., 2008). Temperatures at Kilo Moana reach up to 333^{o}C and depths of 2620 m. The Kilo Moana vent field is surrounded by basaltic substrate host rock dominated by pillow lavas and little sediment cover (Ferrini et al., 2008; Bezos et al., 2009). Bathymetry maps reveal two wide volcanic domes that are cross cut by two well-defined fissures running north-south. The western is measured at 9m deep at 4-20m wide while the eastern fissure is 10m deep and 5m wide. Hydrothermal vent structures are evident adjacent to and at the intersection of both fissures. Hydrothermal activity extends north-south for ~130m with three localized areas of high-temperature venting and diffuse flow. Vent fluids from Kilo Moana are driven through chalcopyrite and wurtzite lined conduits. Fluids diffuse through ~5m tall branches, coalesced pipes, cactus-like protrusions, and beehive-like structures. (Tivey et al., 2005; Seewald et al. 2005; German and Von Damm, 2003).

ABE

Located in the central ELSC region, the ABE vent field is 600 m west of the spreading axis (Figure 5). ABE reaches a maximum depth of 2220 meters with temperatures up to 309^{o}C. ABE is surrounded by pillow and lobate lava host rock with relatively moderate sediment cover. The vent field is dominated by a northeast-southwest oriented fault with parallel steps (Ferrini et al., 2008). At least three identifiable lava flow fronts intersect faulting regions, generating conditions

favorable to hydrothermal activity. ABE consists of three areas of active venting spaced ~85 m apart along dominating fault (Ferrini et al., 2008). Like Kilo Moana, vent fluids are transported through chalcopyrite and wurtzite lined conduits. Fluid exit coalesced pipes, branches, and small chimneys. (Tivey et al., 2005; Seewald et al., 2005).

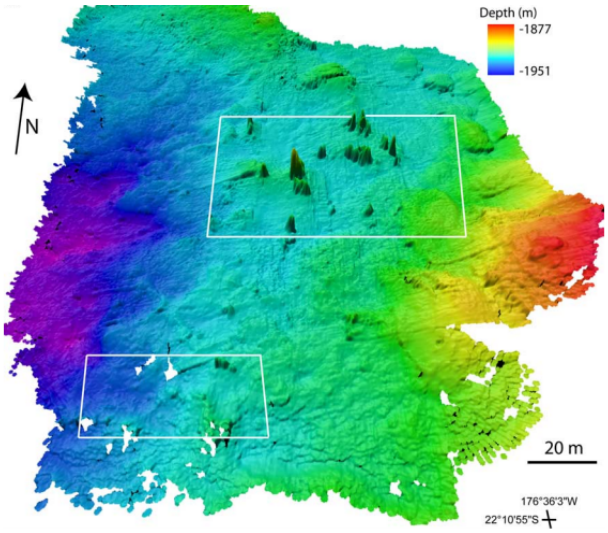

Figure 6: Bathymetry map of Mariner vent site (Ferrini et al., 2008)

Mariner

Located along on the eastern limb of an overlapping spreading center on the Val Fuca Ridge (VFR) section of the southern ELSC, Mariner is the shallowest vent field at 1910m (figure 6). Unlike Kilo Moano and ABE, local faults and fissures are notably absent at Mariner. Heavy sediment cover and felsic host rock ranging from basalt enriched lithophile elements to andesite surrounds Mariner (Jacobs et al., 2007). The vent field is dominated by numerous flat-topped and crater lava domes. Venting at Mariner occurs from the base and sides of 10 to 25m tall and narrow pinnacle structures. High temperature fluids up to 363^{o}C exit through chalcopyrite conduits and porous beehive structures. As opposed to Kilo and ABE, local faults and fissures are notably absent. Higher temperatures, lack of faulting, and abundance of magmatic carbon dioxide (CO_2) suggest that hydrothermal activity at the Mariner vent field is the result of magmatic processes instead of faulting processes. (Tivey et al., 2005; Seewald et al., 2005, Mottl et al., 2011).

As represented in Table 1, Kilo Moana, ABE, and Mariner are vent fields having important differences in: (1) hydrothermal vent formation and activity; (2) relative depth and distance from spreading center; (3) temperature and density of vent field; (4) spreading rates and faulting abundance; (5) chemical composition of vent structures and end member fluids; and (4) overall geologic processes. Therefore, the goals of this thesis are to:

(1) measure the crystalline particle geochemistry of Kilo Moana, ABE, and Mariner hydrothermal plumes;

(2) interpret the particle geochemistry in light of end-member fluid composition and the geological context of the vent field;

(3) develop a data analysis protocol for synchrotron radiation microprobe X-ray diffraction data

Research Approach

Particle-by-Particle X-ray Microprobe Analysis

It is the guiding hypothesis of this thesis that differences in hydrothermal plume particle geochemistry is detectable and correlated with end-member vent fluid composition. In order to properly identify the mineral species and co-located elements that exist in hydrothermal plumesa number of technologies can be utilized. Described here are the two technologies and their associated identification processes that are relevant to this research.

X-ray diffraction (XRD) serves as a powerful tool for researchers to identify mineral species. Diffraction is a physics term used to describe when the wavelength of an electromagnetic wave, such as X-rays, is reflected causing the wave to change direction without changing speed. In mineralogy, mineral samples are subjected to X-rays and diffraction is observed when the spacing between atomic layers in a crystal is approximately equal to the wavelength of the X-ray photons. In 1913, English physicist Sir W.H. Bragg derived an equation to explain why the cleavage faces of crystals appear to reflect X-ray at certain angles of incidence (Equation 1).

$$n\lambda = 2d \sin\Theta \qquad (1)$$

Where n equals an integer, λ equals the wavelength of the incident X-ray beam, d equals the distance between atomic layers in a crystal, and Θ equals the angle of incidence an X-ray beam creates with the horizontal samples. The result is a Bragg diffraction pattern is formed from constructive interference of X-rays by the regular three-dimensional arrangement of atoms in the solid. The diffraction pattern, plotted as intensity versus two-theta, can be compared to a database of reference patterns to properly identify minerals.

Powder diffraction is a specific category of XRD investigation in which the sample is analyzed in powder form. During powder diffraction the incident energy interacts with many, perhaps hundreds of thousands, small crystals that are in all possible orientations relative to the incident X-rays—therefore, satisfying all Bragg diffraction conditions as the incident X-ray angle is systematically varied and measuring the whole of the mineral structure. Powder diffraction analysis is especially powerful in natural samples that are fine grained (not single particle or single crystal) and relatively homogeneous. For the heterogeneous samples considered in this research, a synchrotron radiation microprobe X-ray diffraction technique was

used to isolate diffraction signatures from individual particles or aggregates. The advantage of this approach is that the data are simplified by having co-located elemental information (described below) and fewer diffracting phases per diffractogram. The main disadvantage is that the XRD data are collected with a single incident energy, i.e. there is no goniometer, and it is rare to find particle(s) that will satisfy all Bragg diffraction conditions with this sample-detector geometry. In response to this challenge, a detailed peak identification protocol has been developed for the ELSC plume particle samples.

X-ray fluorescence (XRF) is the radiative emissions from a material that has been exited through the bombardment of X-rays at specific wavelengths. By exposing a material to X-rays above but near the absorption energy of an element, photons are absorbed by the atom and electrons are promoted in quantized steps that can result in the ejection of photo-electrons from the atom. Removal of an electron renders the electronic structure of the atom unstable, thus causing higher orbital electrons to "fall" in order to fill missing electron's place. During this process, energy is released in the form of fluorescence at characteristic wavelengths. This release of energy can be measured to determine which elements are present in a material, due to their unique electronic structure and fluorescence energies. Using multiple incident energies and an x-y scanning sample stage, a large number of elements (sulfur to arsenic) can be measured by fluorescence using an X-ray microprobe. The final product, an XRF map, demonstrates the relative concentration and distribution of elements within a sample. XRF mapping of hydrothermal plume samples is important for properly identifying minerals based on XRD peak matching.

This study examines the particle geochemistry of Kilo Moana, ABE, and Mariner vent fields. Through the use of microprobe XRF and XRD, the mineralogical analysis will provide a site-by-site comparison of the hydrothermal plumes. It is hypothesized that differences in the geochemical composition of hydrothermal particulates is detectable due to the diversity in local hydrology, geology, and chemistry.

Methods

During the 2008 research cruises of the R/V Thomas G. Thompson (TN235 and TN236), rising plume particulate samples were collected along the ELSC using the SUPR sampler deployed on ROV *Jason II*.

Sampling Equipment Cleanliness

All sampling components were cleaned prior to the cruise by a combination of 5% ethanol and trace-metal clean 5% HCl (Seastar) baths. All plastic ware was rinsed with MQ water, and leached with 10% HCl (Seastar) at pH 2, and sample bottles were rinsed with sample prior to sample collection. All critical cleaning was done in the Saito clean room at WHOI, which exceeds Class-100 standards.

Sample Collection and In Situ Data

Target vents were approached along the seafloor using the state-of-the-art navigation techniques for the *Jason II* ROV. For each vent, near bottom background samples were taken in the vicinity of the vent but outside of the plume (> 3 m distance). The manipulator was then used to position the SUPR sampler intake directly within the rising plume at a height of ~0.5 m above the vent orifice, a position from which 2 geochemical samples were collected. An operator controlled in situ filtered water volumes collected. During sampling, the most reliable means of positioning the sampler intake within the plume were visual using aimed red lasers that illuminated plume particles. Variability due to turbulence was encountered in plume flow over the sampling time, but this variability is reduced in our samples by integration during the 10-30 min required to collect each SUPR sample. Water samples for shipboard pH, total Fe and Mn, and dissolved nutrients were also collected from the neutrally buoyant plume at every site.

Sample Handling

All pre-deployment filter handling was performed within a shipboard fabricated polyethylene enclosure; and all post-deployment shipboard and laboratory filter handling was performed in an argon-purged glovebox. Acid cleaned in 10% Seastar HCL, pre-weighed, 37 mm diameter, 0.8 μm poresize polycarbonate (GE Osmonics) filters were used for all trace-metal and X-ray micro-spectroscopy samples. Upon recovery the samples for geochemical analysis were rinsed with distilled/deionized water, neutralized with trace metal grade ammonia, to remove sea salts, transferred to vacuum storage containers within the argon glove box, and frozen under vacuum until analysis. Water samples for Fe and Mn analysis were acidified to a pH of 1.7 with high purity HCl (Seastar), and were stored in trace metal clean, low-density polyethylene bottles at room temperature for several months to dissolve metals adhered to bottle walls. In the laboratory, particle samples for geochemical analysis were dried, post-weighed on a Perkin-Elmer AD 6 microbalance, and when necessary split with Teflon scissors in an argon purged glove box. Filter splitting is performed gravimetrically. Splits for X-ray synchrotron analysis were shipped frozen under vacuum to the Advanced Light Source for analysis.

Micro-beam X-ray Fluorescence Mapping and Diffractions

Plume particles were exposed to X-ray microprobe measurements at the Advanced Light Source, Lawrence Berkeley National Laboratory, Berkeley, CA, USA, at beamline (BL) 10.3.2 (Marcus et al., 2004). A total of 67 points, including filter backgrounds, were selected for spectroscopy and diffraction analysis based particle density, co-located elements, and regions of interest. Data collection at BL 10.3.2 on filter-bound plume particles had the following task flow: (1) X-ray fluorescence (XRF) mapping at multiple energies to determine the spatial distribution of elements in the particles within a region of interest, and (2) X-ray diffraction (XRD) measurements at all particles/aggregates of interest following XRF mapping.

X-ray Fluorescence (XRF)

Approximately one hour prior to analysis, an original polycarbonate membrane filter hosting particle plumes was defrosted and mounted to aluminum sample holders. Plume particles were subject to ambient temperatures and pressures during x-ray microprobe measurements. X-ray fluorescence (XRF) mapping was preformed at multiple energies to determine the spatial distribution of elements in the particles at XRD locations. Five separate incident energies were used at each location:

1. "17keV" map with incident energy set to 17,000 eV providing distribution of Fe, Ni, Cu, Zn, and As elements
2. "Fe_minus" map with incident energy set to 2,000 eV providing Mn distribution without interference from Fe Kα fluorescence emissions
3. "Vk_Plus" map with incident energy set to 200 eV in order to distinguish V Kα from Ti Kβ fluorescence emission
4. "V_minus" map with incident energy set to 200 eV provided distribution of Ti and Ca
5. Maps for Si, S, Cl and K were typically obtained from the lowest energy map collected

Five incident energies were collected at 57 of the 67 sample points. The remaining 10 points on the Mariner sample filter (labeled 16-26) only underwent 17keV incident energy. This was due to a lack of collection time at the 10.3.2 beamline.

X-ray Diffraction (XRD)

X-ray diffraction patterns were collected at an incident energy of 17 keV (λ=0.729 angstrom) with 240-second exposure, with a spot size of 6 × 11 μm. The XRD patterns were

radially integrated to obtain profiles as intensity versus 2θ using the freeware Fit2D after calibration of sample-to-detector distance with data from an Al_2O_3 (alumina standard) (Hammersley et al., 1996). Background filter XRD scans were collected for each of the three filters. After analysis, samples were returned to an argon filled box, sealed into mylar bags with oxygen scrubbers (AnaeroPack-Anero; Mitsubishi Gas Chemical Co., Inc.) and frozen for shipping and storage.

Software Analysis

Individual XRF maps were deadtime corrected, aligned, and channels of interest were added to a single composite map using custom beamline software (Marcus et al., 2004). Graph-interpreted XRF peaks were individually measured and matched to their associated elements. Background filter scans were additionally measured for comparison.

Sampled XRD patterns underwent JADE software peak analysis (Materials Data Inc). After radial integration using freeware Fit2D, profiles of intensity versus 2θ files were imported into JADE through the manual adjustment of import conditions. Resulting XRD-detected samples produced a moving average pattern for each individual point. Background filter XRD patterns were displayed and individually subtracted from each sample pattern. Additional background noise detected by JADE was subtracted to produce a uniform baseline for the XRD patterns. Sampled patterns underwent peak identification using the mineral standards of MDI-500 and AMCS databases. In addition, a chemistry-filter tool in JADE was utilized to discourage the identification of any nonexistent elements in deep-sea environments—for example, Fermium (Fm). Peak identification process by JADE, including chemistry filter steps, produced a list of possible standard-to-sample mineral matches. Each listed match was quantitatively assigned a Figure of Merit (FOM) number based on the quality of match; this FOM number is used during the final best-fit analysis.

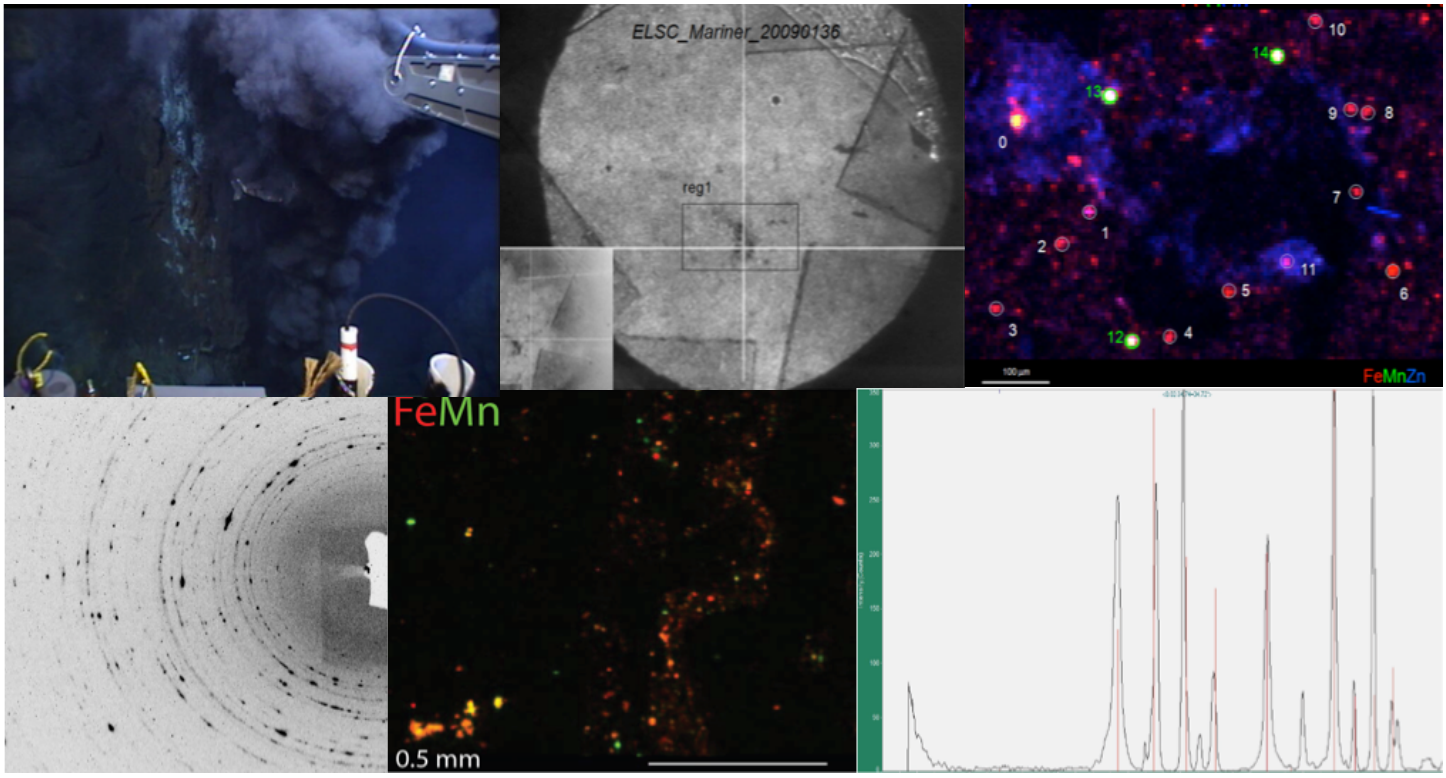

Figure 7 (top left): *SUPR sampler* deployed on *ROV Jason* robotic arm collecting 0.5m hydrothermal plume samples (Brier et al., 2009). Figure 8 (top center): SUPR sampler filter displaying collected plume particles. Figure 9 (top right): Filter sample designating XRD and XRF "spots" to be analyzed. Figure 10 (bottom left): resulting pattern as shown from XRD detector. Figure 11 (bottom center): XRF mapping identifying iron and manganese in an individual spot. Figure 12 (bottom right): JADE XRD analysis (Materials Data Inc.) identifying Pyrite (FeS_2) in spot 14 of ABE 0.5m sample

Best-fit analysis

Analyzing XRD mineral data from naturally collected samples poses a number of challenges. First, particle aggregates containing multiple mineral species may result in complex XRD signals. Second, the sample-detector geometry is fixed during XRD data collection and randomly oriented particles of a single phase are not commonly observed for these samples. This means that the XRD patterns with numerous peaks rarely contain all possible Bragg diffraction peaks for a mineral and the relative intensity ratios between peaks observed for random powder diffraction may be significantly altered. Finally, many minerals (or phases) within these samples lack long-range structural order and do not produce strong Bragg diffraction patterns, so these phases are at best difficult to identify with confidence and at worst not detected. Therefore, this project addresses the crystalline minerals within the hydrothermal

plume. Due to these complications, standard protocols for XRD pattern identification did not work well for most of our data, and method development was required. A description of this new method is provided below.

JADE automatically assigns each potential mineral with a Figure of Merit (FOM) number. A FOM number (or rating) of zero represents a perfect sample-to-standard correlation, thus concluding the mineral identity of the filter-bound particle. Conversely, a FOM rating of 25.0 or higher represents an imperfect standard-to-sample match due to missing, oversized, or offset peaks from pattern. In order to classify potential minerals, a *best-fit* point system was developed so that they may be ranked accordingly.

Points System

2 - Two points were designated to potential minerals with an assigned FOM of 25.0 or below

1 - One point was designated to potential minerals with an assigned FOM 25.1 or above

1 - One additional point was given to potential minerals that correspond with XRF identified elements

Designated points from each potential mineral were combined to form a *best-fit* score. A maximum *best-fit* score of 3 represents a highly confident mineral identification. This score is used to rank identified minerals based on the likelihood of their existence.

Results

Complete data tables can be found in the supplemental information section. The following identified minerals are separated in table 2 into correspond to their respective hydrothermal vent site. Numbers listed before minerals indicate the frequency of occurrence. Mineral species are ordered according to *best-analysis* criteria:

Very confident- JADE identifies a strong XRD mineral match (FOM≤25) and corresponding elements are detected in XRF data

Confident- JADE identifies a strong XRD mineral match (FOM≤25); *or* JADE identifies an approximate XRD mineral match (FOM≥25) and corresponding elements are detected in XRF data

Less confident- JADE identifies an approximate XRD mineral match (FOM≥25)

Kilo Moana

Very Confident	*Confident*	*Less confident*
3- Pyrite (FeS_2)	Pyrite (FeS_2)	Chromate aluminate ($Ca_4Al_6CrO_{15}$)
Stannoidite ($ZnFe_2Cu_8Sn_2S_{12}$)	Rudashevskyite (FeS)	Magnesite ($MgCo_2$)
Wurtzite (ZnS)	Bornite (CuFeS)	Spinel ($(Al_2Mg)O_3$)
	Kesterite (Cu_2ZnSnS_4)	Coesite (SiO)
	Lautite (CuAsS)	

ABE

Very Confident	*Confident*	*Less confident*
7- Pyrite (FeS_2)	IronSulfide (FeS)	2- Langbeinite ($K_2Ca_2(SO_4)_3$)
3- Sphalerite (ZnS)	Pyrite (FeS_2)	Cristobalite (SiO_2)
3- Sulfur (S)	Chalcocite (Cu_2S)	
Hematite (Fe_2O_3)	Schulenbergite ($(Cu_5Zn)S_2O_{21}H_{36}$)	
Wurtzite (ZnS)	Grossular ($Ca_3FeSi_3O_{12}$)	
Chalcocite (Cu_2S)	Lautite ($K_2Ca_2(SO_4)_3$)	
	Akermite ($Ca_2CoSi_2O_7$)	
	Quartz (SiO_2)	
	Halite (NaCl)	

Mariner

Very Confident	*Confident*	*Less confident*
5-Chalcopyrite ($CuFeS_2$)	2- Sulfur (S)	Manganite (MnO(OH))
4- Pyrite (FeS_2)	Apatite ($Ca_5P_3O_{12}F$)	
3- Fluorite (CaF_2)	Nickel silicide ($NiSi_2$)	
2- Apatite ($Ca_5P_3O_{12}F$)	Apatite ($Ca_5P_3O_{12}F$)	
Sphalerite (ZnS)	Fluorite (CaF_2)	
Grattarolite (Fe_3PO_7)	Lithium (Li)	
Franklinite ($(Fe,Zn)_2O_4$)	Periclase (MgO)	
Trioilite (FeS)	Molysite ($FeCl_3$)	
Titanium (Ti)*	Iron titanium sulfide ($FeTi_3S_6$)	

Table 2: Minerals successfully identified by JADE XRD data, supported by XRF mapping, and best-fit analysis. *Very confident* represents JADE identified strong XRD mineral match (FOM≤25) and corresponding elements detected in XRF data. *Confident* represents JADE identified strong XRD mineral match (FOM≤25); *or* JADE identified an approximate XRD mineral match (FOM≥25) and corresponding elements are detected in XRF data. *Less confident* represents an approximate JADE XRD mineral match (FOM≥25)

Discussion

The bottom profile plume particles of three hydrothermal vents—Kilo Moana, ABE, and Mariner—were sampled over a 241 km stretch of the ELSC. A southward convergence of the ELSC and the Tofua arc volcanic front generates an increasing influence of the arc and subducted slab on the composition and structure of the ridge crest from north to south. In addition, each vent site exhibits unique substrate, large-scale magmatic processes, chimney composition, and bulk-chemistry.

Kilo Moana, located in the northern ELSC, is surrounded by back-arc basin basalt at 2620 depth. Spreading rates at Kilo Moana are fast, the crust is relatively thin, faults are abundant and large, and a magma lens is absent. ABE is located on the central ELSC at a depth of 2220m and is surrounded by basaltic andesite. The spreading rate, abundance of faulting, and crustal thickness at ABE is relatively intermediate. Mariner is located on the southern end of the ELSC and is surrounded by both basaltic andesite and more felsic rocks. Reaching depths of 1910 m, Mariner is characterized with slower spreading rates, a thick crust, and a deep magma lens. Most notable is the lack of faults and fissure at Mariner, suggesting magmatic processes involved in hydrothermal activity (Tivey et al., 2005; Seewald et al., 2005; Mottl et al., 2011).

Submarine hydrothermal fluids examined in this study reflect the integrated effects of reaction between seawater and ocean lithosphere rock. The type and magnitude of chemical

exchange associated with this reaction is influenced by the many variables, including temperatures, pressure, rock composition, and subsurface hydrology. Overall, substantial differences in the physical and chemical conditions along the ELSC are expected to influence the composition of end-member hydrothermal fluids.

Major Species Detected

Reduced metal species were detected in the form of polymetallic sulfides in each plume. The observation of the sulfide species reinforces the current model of hydrothermal plume chemistry, which predicts sulfide precipitation in the lower plume (Brier et al., 2012). Additionally, the concentration of the reduced metals observed coincide with previous bulk-chemistry research (Mottl et al., 2011). For example, Fe, Mn, Cu, Zn, were all previously found at 0.003-7100 mm/kg above standard seawater levels by Ishibashi and Urabe (1995). The appearance of these reduced elements in sampled minerals therefore supports their accurate identification.

Iron sulfides, particularly pyrite, are the dominant mineral species at all plumes. It is hypothesized that the increasing patterns of variation in Fe from north to south are correlated with decreasing pH. Mariner, with the lowest measured pH relative to northern sites, displays a wide variety of Fe mineral species relative northern vent sites—chalcopyrite ($CuFeS_2$), Pyrite (FeS_2), Grattarolite (Fe_3PO_7), Franklinite ($(Fe,Zn)_2O_4$), and Trioilite (FeS) (Mottl et al., 2011).

Although manganese is present in deep-sea hydrothermal vent fluids, (12-7100 mm/kg above standard seawater levels) only one manganese mineral phase was identified in the sample set. We suggest that a lack of identified manganese phases is due to three factors: (1) XRD may be unable to detect trace amounts of Mn mineral phases; (2) Mn is usually much slower to precipitate with sulfides than iron and other reduced metals, thus remaining partially dissolved in the lower plume profile; and (3) manganese oxides and hydroxides are often poorly crystalline and therefore difficult to detect via XRD (German and Von Damm, 2003).

Major Trends

Discrepancies between vent sites are observed in mineral species. Dissolved SiO_2 is observed both at Kilo and ABE, while absent at Mariner. A decreasing trend in SiO_2 abundance consistent with the southerly decrease in depth along the ELSC. Presence of aqueous SiO_2 is controlled by quartz solubility, which increases greatly with pressure due to increasing seafloor depth (Seyfried, 2003). Silica-bearing (Si) minerals are present at each vent site, but drastically increase at ABE. Increasing abundance of Si is attributed to an increasing presence of silicic magma at ABE (Mottl et al., 2011).

There is an increasing abundance in calcium-bearing minerals from north to south, excluding

the “less-confident” phases. This observation is consistent with bulk-chemistry findings by Mottl et al., 2011. Large calcium (Ca) to chloride (Cl) ratios have been previously attributed to the degree of phase-separation during subsurface water-rock interaction. Although there is a lack of Cl in identified minerals, this hypothesis may explain an increase in Ca towards the high-temperature, magmatic-driven Mariner site.

Another notable trend is the abundant concentration of chemicals associated with the chimney composition at each vent site. A large presence of chalcopyrite ($CuFeS_2$) is unique to Mariner only. Conversely, wurzite (ZnS) is only present at ABE and Kilo Moana. It is hypothesized that there is a correlation between vent chimney composition and 0.5 meter end-member fluid; vent chimneys at Mariner consist of chalcopyrite, while Kilo Moana and ABE consist of a wurzite-chalcopyrite mix. It is possible that pieces of the chimney were expelled with end-member fluid and collected in samples.

Site-specific Observations

There is an increase particulate matter abundance of potassium (K) bearing minerals identified at ABE vent site. The presence of potassium may be attributed to the mixed basalt and andesite substrate composition found at ABE (Mottl et al., 2011).

There is an interesting increase in fluoride (F) abundance identified at Mariner. Previous research has attributed increasing F concentrations with an increase of subducted sediment (Mottl et al., 2011). A north to south increase in amount of sediment, with Mariner exhibiting the highest degree of sediment cover, may explain why F-bearing minerals are concentrated at Mariner alone.

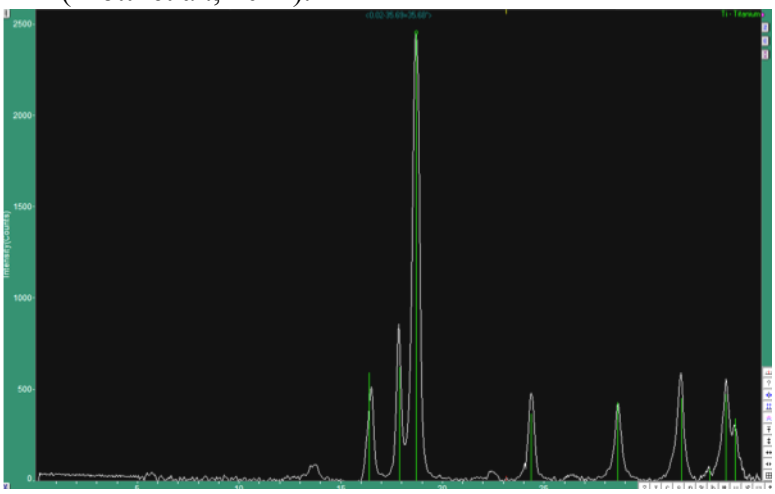

Figure 13: Titanium phase as identified by JADE (Materials Data Inc.)

Surprising Phases

The titanium XRD phase at Mariner (Figure 13) exhibits a near-perfect match to pure titanium. It is hypothesized that this titanium originates from the *ROV Jason* titanium robotic arm. This conclusion is supported by a lack of titanium concentrations associated with hydrothermal vent fluids (Tivey et al., 2007).

Conclusion

Submarine hydrothermal fluids represent the integrated effect of seawater and host-rock interaction within the local seafloor and are influenced by depth, tectonic parameters, magmatic properties, and proximity to the subducting arc. The Kilo Moana, ABE, and Mariner hydrothermal vent fields of the Eastern Lau Spreading Center were studied due to the fact they are spatially close yet exhibit a variety of hydrothermal fluid compositions.

In this study we used XRD and XRF analysis to identify mineral speciation within hydrothermal plume particles. Metal-rich Fe sulfide minerals, particularly pyrite, were present and represented the predominant crystalline phases at all three sites. However, chalcopyrite was only identified at the Mariner site and wurtzite was only identified at Kilo Moana and ABE; indicating that the chemical characteristics of lower-plume profiles can be unique to vent site from which they originate.

These findings reinforce previous bulk-chemistry research, as well as validate the current understanding of hydrothermal vent chemistry. Additionally, the location specific variations in mineral species provide important new insights into the specific processes that control the chemistry of hydrothermal vent systems.

Supplemental Information Complete XRD and XRF results. Phases with no mineral matches are omitted.

Vent Identification	Sample Height (m)	Best Fit Score	Spot #	XRD Mineral Detected	Chemical Formula	XRF elements detected	FOM
Kilo Moana	**0.5**	3	10	Stannoidite	Zn.85Fe2.15Cu8Sn2S12	S; V; Fe; Zn	9.4
		2	10	Lautite	CuAsS	S; V; Fe; Zn	11.6
		2	12	Kesterite	Cu2ZnSnS4	S; V; Fe; Zn	7.5
		3	13	Pyrite	FeS2	S; Ca; V; Fe; Cu; Zn	16.6
		3	14	Pyrite	FeS2	S; Ca; V; Fe; Cu; Zn	16.7
		3	15	Wurtzite	ZnS	S; Ca; V; Fe; Cu; Zn	24.4
		3	16	Pyrite	FeS2	S; V; Fe; Zn	10.1
		2	10	Coesite	SiO	S; V; Fe; Zn	9.9
		2	11	Bornite	Cu1.25Fe.25S	S; V; Fe; Zn	58.5
		2	14	Rudashevskyite	(Fe/Zn/Mn)S	S; Ca; V; Fe; Cu; Zn	30.6
		2	15	Pyrite	FeS2	S; V; Fe; Cu; Zn	102.4
		1	0	Chromate aluminate sodalite	Ca4Al6CrO15	S; V; Fe; Cu; Zn	26.8
		1	8	Magnesite	MgCo2	S; V; Fe; Zn	75
		1	11	Spinel	(Al2Mg)O3	S; V; Fe; Zn	47.4
		1	11	Manganese (II)	MnSn(O6H6)	S; V; Fe; Zn	55.9
			20	background	background	V; Fe; Zn	
Mariner	**0.5**	3	3	Fluorite	CaF2	Fe; Cu; Zn; Cl; Ca; Mn; V	3.8
		3	5	Fluorite	CaF2	Fe; Cu; Zn; Cl; Ca; Mn; V	9.1
		3	6	Sphalerite	ZnS	Zn; S; Fe; Ca; V	6.7
		3	7	Fluorite	CaF2	Fe; Zn; Ca; V	2.6
		3	7	Pyrite	FeS2	Fe; Zn; Ca; V	3.7
		3	8	Pyrite	FeS2	Fe; Ca; Mn	2.2
		3	12	Apatite	Ca5P3O12F	Cl; Fe; V; Ca	3.1
		3	13	Titanium	Ti	Ti; Cl	2.1
		3	14	Apatite	Ca5P3O12F	Ca; Fe; Mn; V	7.9
		3	15	Pyrite	FeS2	Fe; S; Ca; Mn; V	4.9

		3	16	Chalcopyrite	CuFeS2	Fe; Cu; Zn	4.9
		3	17	Chalcopyrite	CuFeS2	Fe; Cu	16.2
		3	20	Grattarolaite	Fe3PO7	Fe, Zn	18
		3	20	Iron titanium sulfide	FeTi3S6	Fe, Zn	14
		3	21	Chalcopyrite	CuFeS2	Fe, Cu, Zn	8
		3	21	Pyrite	FeS2	Fe, Cu, Zn	9
		3	24	Chalcopyrite	CuFeS2	Fe, Cu, Zn	11.9
		3	25	Chalcopyrite	CuFeS2	Fe, Cu, Zn	15.1
		3	26	Trioilite	FeS	Fe, Zn	15.9
		3	26	Franklinite	(Fe,Zn)2O4	Fe, Zn	23
		2	3	Sulfur	S	Fe; Cu; Zn; Cl; Ca; Mn; V	6.9
		2	6	Nickel Silicide	NiSi2	Zn; S; Fe; Ca; V	4.3
		2	5	Apatite	Ca5P3O12F	Fe; Cu; Zn; Cl; Ca; Mn; V	8.3
		2	20	Fluorite	CaF2	Fe, Zn	9
		2	20	Lithium	Li	Fe, Zn	5
		2	21	Periclase	MgO	Fe, Cu, Zn	8.9
		2	21	Sulfur	S	Fe, Cu, Zn	9.3
		2	24	Molysite	FeCl3	Fe, Cu, Zn	99.3
		1	17	Manganite	MnO(OH)	Fe; Cu	38.8
			22	background		none	
Abe	**0.5**	3	0	Pyrite	FeS2	S; Mn; Fe; Cu; Zn; As	3.7
		3	0	Sulfur	S	S; Mn; Fe; Cu; Zn; As	8.1
		3	1	Pyrite	FeS2	S; Mn: Fe; Cu; Zn; As	4
		3	1	Sphalerite	ZnS	S; Mn: Fe; Cu; Zn; As	16.1
		3	1	Sulfur	S	S; Mn: Fe; Cu; Zn; As	8.1
		3	2	Pyrite	FeS2	Fe; Cu; Zn; As	13.4
		3	2	Sphalerite	ZnS	Fe; Cu; Zn; As	16.1
		3	2	Sulfur	S	Fe; Cu; Zn; As	8.8
		3	4	Hematite	Fe2O3	Fe; Zn	19.6
		3	5	Pyrite	FeS2	Mn; fe; Cu; Zn; As	4.7
		3	6	Sphalerite	ZnS	Fe; Cu: Zn; As	7

		3	6	Pyrite	FeS2	Fe; Cu: Zn; As	20.6
		3	6	Chalcocite	Cu2S	Fe; Cu: Zn; As	15.5
		3	15	Pyrite	FeS2	Ca; Fe; Cu; Zn	18.3
		3	15	Wurtzite	ZnS2	Ca; Fe; Cu; Zn	11
		3	16	Pyrite	FeS2	Fe; Cu: Zn	2.7
		2	7	Chalcocite	Cu2S	Ca; Mn; Fe; Cu: Zn; As	99.9
		2	8	Schulenbergite	(Cu5Zn)S2O21H36	Cl: Ca; Mn: Fe; Cu; Zn	59.2
		2	9	Grossular	Ca3(Al,Fe)Si3O12	Cl: Ca; Mn: Fe; Cu; Zn	68
		2	10	Quartz	SiO**2**	Cl; Ca;Mn; Fe; Cu: Zn	21
		2	10	Halite	NaCl	Cl; Ca;Mn; Fe; Cu: Zn	36
		2	11	IronSulfide	FeS	Ca; Fe; Cu; Zn	88.9
		2	14	Pyrite	FeS2	Fe; Cu; Zn	26.6
		2	19	Lautite	K2Ca2(SO4)3	Cl; Ca; Fe: Cu; Zn	40
		2	19	Akermite	Ca2CoSi2O7	Cl; Ca; Fe: Cu; Zn	74
		1	12	Langbeinite	K2Ca2(SO4)3	Fe; Cu; Zn	74
		1	13	Langbeinite	K2Ca2(SO4)3	Fe; Cu; Zn	75.4
		1	14	Cristobalite	SiO2	Fe; Cu; Zn	39.4

References

Baker, E. T., G. J. Massoth, K. Nakamura, R. W. Embley, C. E. J. de Ronde, and R. J. Arculus (2005), Hydrothermal activity on near-arc sections of back-arc ridges: Results from the Mariana Trough and Lau Basin, *Geochem. Geophys. Geosyst*. **6**(9), Q09001

Baker, E. T., J. A. Resing, S. L. Walker, F. Martinez, B. Taylor, and K. Nakamura (2006), Abundant hydrothermal venting along melt-rich and melt-free ridge segments in the Lau back-arc basin, *Geophys. Res. Lett*. **33**, L07308,

BeÅLzos A., Escrig S., Langmuir C. H., Michael P. J. and Asimow P.D. (2009) Origins of chemical diversity of back-arc basin basalts: a segment scale study of the Eastern Lau Spreading Center. *J.Geophys. Res*. **114**, B06212.

Brier et al. (2012) Sulfur, sulfides, oxides and organic matter aggregated in submarine hydrothermal plumes at 9°50'N East Pacific Rise. *Geochimica et Cosmochimica Acta*. **88**, 216-236.

Breier J. A., Rauch C. G., McCartney K., Toner B. M., Fakra S. C., White S. N. and German C. R. (2009) A suspended-particle rosette multi-sampler for discrete biogeochemical sampling in low-particle-density waters. *Deep Sea Res. Pt. I* **56**, 1579–1589.

Cowen J. P., Bertram M. A., Wakeham S. G., Thomson R. E., Lavelle J. W., Baker E. T. and Feely R. A. (2001) Ascending and descending particle flux from hydrothermal plumes at Endeavour Segment, Juan de Fuca Ridge. *Deep Sea Res. Pt. I* **48**, 1093–1120.

Edmond J. M., Measures C., McDuff R. E., Chan L. H., Collier R., Grant B., Gordon L. I. and Corliss J. B. (1979) Ridge crest hydrothermal activity and the balances of the major and minor elements in the ocean: the Galapagos data. *Earth Plan. Sci. Lett.* **46**, 1–18.

Elderfield H. and Schultz A. (1996) Mid- ocean ridge hydrothermal fluxes and the chemical composition of the ocean. *Annu. Rev. Earth Planet. Sci.* **24**, 191–224.

Ferrini V. L., Tivey M. K., Carbotte S. M., Martinez F. and Roman C. (2008) Variable morphologic expression of volcanic, tectonic, and hydrothermal processes at six hydrothermal vent fields in the Lau back-arc basin. Geochem. Geophys. Geosystems **9(**7**).**

Fouquet Y., von Stackelberg U., Charlou J. L., Erzinger J., Herzig P. M., Muhe R. and Wiedicke M. (1993) Metallogenesis in back-arc environments: the Lau Basin example. *Econ. Geol*. **88**, 2154–2181.

German, C. R., D. P. Connelly, R. D. Prien, D. R. Yoerger, M. Jakuba, A. M. Bradley, T. Shank, K. Nakamura, C. H. Langmuir, and L. M. Parsons (2005), New techniques for hydrothermal plume investigation by AUV, *Geophys. Res*. Abstr., 7,

German C. R. and Vonn Damm K. L. (2003) Hydrothermal processes. *Treatise on Geochemistry* **6**, 181 – 222.

Hammersley A. P., Svensson S. O., Hanfland M., Fitch A. N. and Hausermann D. (1996) Two-dimensional detector software: from real detector to idealized image or two-theta scan. *High.Press. Res.* **14**, 235–248.

Haymon R. M., Fornari D. J., Von Damm K. L., Lilley M. D., Perfit M. R., Edmond J. M., Shanks W. C., Lutz R. A.,Grebmeier M., Carbotte S., Wright D., McLaughlin E., Smith M., Beedle N. and Olson E. (1993) Volcanic-eruption of the midocean ridge along the East Pacific Rise crest at 9_45–52**0**N – direct submersible observations of sea-floor phenomena associated with an eruption event in April, 1991. *Earth Planet. Sci. Lett.* **119**, 85–101.

Ishibashi, J., J. E. Lupton, T. Yamaguchi, J. Querellou, T. Nunoura, and K. Takai (2006), Expedition reveals changes in Lau Basin hydrothermal system, *Eos Trans.* AGU, **87**(2), 13,

Ishibashi J.-I., and T. Urabe T. 1995. Hydrothermal activity related to arc-backarc magmatism in the western Pacific. Backarc Basins:Tectonics and Magmatism. Pp. 451-495 in B. Taylor, ed., Plenum,New York, NY.

Jacobs A. M., Harding A. J. and Kent G. M. (2007) Axial crustal structure of the Lau back-arc basin from velocity modeling of multichannel seismic data. Earth. *Planet. Sci. Lett.* **259**, 239–255.

Lupton J. E., Delaney J. R., Johnson H. P. and Tivey M. K. (1985) Entrainment and vertical transport of deep-ocean water by buoyant hydrothermal plumes. *Nature* **316**, 621–

623.Marcus M. A., MacDowell A., Celestre R., Manceau A., Miller T., Padmore H. A. and Sublett R. E. (2004) Beamline 10.3.2 at ALS: a hard X-ray microprobe for environmental and material sciences. J. *Synchrotron Rad.* **11**, 239–247.

Martinez F., Taylor B., Baker E. T., Resing J. A. and Walker S. L. (2006) Opposing trends in crustal thickness and spreading rate along the back-arc Eastern Lau Spreading Center: implications for controls on ridge morphology, faulting, and hydrothermal activity. *Earth Planet Sci. Lett*. **245**, 655–672.

Mottl M. J., Seewald J. S., Wheat C. G., Tivey Margaret K., Michael P. J., Proskurowski G., McCollom T. M., Reeves E., Sharkey J. and You C.-F. (2011) Chemistry of hot springs along the Eastern Lau Spreading Center. *Geochimica et Cosmochimica Acta* **75**, 1013–1038.

Mottl M. J. and Wheat C. G. (1994) Hydrothermal circulation through mid-ocean ridge flanks: Fluxes of heat and magnesium. *Geochimica et Cosmochimica Acta* **58**, 2225–2237.

Pearce, J. A., M. Ernewein, S. H. Bloomer, L. M. Parson, B. J. Murton, and L. E. Johnson (1995), Geochemistry of Lau Basin volcanic rocks: Influence of ridge segmentation and arc proximity, in Volcanism Associated With Extension at Consuming Plate Margins, *Geol. Soc. Spec. Publ.,* **81**, 53 – 75.

Proskurowski, G., J. S. Seewald, E. Reeves, T. M. McCollom, J. Lupton, S. Sylva, and M. K. Tivey (2007), Volatile chemistry at Lau Basin hydrothermal sites: Basin-wide trends of slab carbonate influence and suggestions of abiotic methane oxidation at the Mariner vent site, *Eos Trans.* AGU, **88**(52), Fall Meet. Suppl., Abstract V34B-04.

Seewald, J., T. McCollom, G. Proskurowski, E. Reeves, M. Mottl, J. Sharkey, C. G. Wheat, and M. Tivey (2005), Aqueous volatiles in Lau Basin hydrothermal fluids, *Eos Trans*. AGU, **86**(52), Fall Meet. Suppl., Abstract T31A-0478.

Seyfried, Jr., W. E., Berndt M. E. and Seewald J. S. (1988) Hydrothermal alteration processes at mid-ocean ridges: constraints from diabase alteration experiments, hot-spring fluids and composition of the oceanic crust. *Can. J. Earth Sci*. **26**, 787–804.

Seyfried, Jr., W. E., Seewald J. S., Berndt M. E., Ding K. and Foustoukos D. (2003) Chemistry of hydrothermal vent fluids from the Main Endeavour Field, Northern Juan de Fuca Eidge: geochemical controls in the aftermath of the June 1999 seismic events. *Geophys. Res*. **108**, 2429–2452.

Tagliabue, A., Bopp, L., Dutay, J.-C., Bowie, A. R., Chever, F., Jean-Baptiste, P., Bucciarelli, E., Lannuzel, D., Remenyi, T., Sarthou, G., Aumont, O., Gehlen, M., and Jeandel, C., 2010. Hydrothermal contribution to the oceanic dissolved iron inventory. *Nature Geoscience* **3**, 252-256.

Tivey M.K. (2007) Generation of seafloor hydrothermal vent fluids and associated mineral deposits. *Oceanography* **20**, 50–65. http://darchive.mblwhoilibrary.org:8080/handle/1912/2775

Tivey, M. K., P. Craddock, J. Seewald, V. Ferrini, S. Kim, M. Mottl, A. Sterling, A.-L. Reysenbach, C. G. Wheat, and the TUIM05MV Scientific Party (2005), Characterization of six vent fields within the Lau Basin, *Eos Trans.* AGU, **86**(52), Fall Meet. Suppl., Abstract T31A-0477

Von Damm K. L. (1995) Controls on the chemistry and temporal variability of seafloor hydrothermal fluids. In S. E. Humphris, R. A. Zierenberg, L. S. Mullineaux and R. E. Thomson (eds.), Seafloor Hydrothermal Systems: Physical, Chemical, Biological, and Geological Interactions. *Geophys. Mono. 91, Amer. Geophys. Union*, 222–247.

Zellmer, K. E., and B. Taylor (2001), A three-plate kinematic model for Lau Basin opening, Geochem. *Geophys. Geosyst.,* **2**(5), 1020